Vision Research 51 (2011) 1835–1844

Contents lists available at ScienceDirect

Vision Research

journal homepage: www.elsevier.com/locate/visres

Imaging retinal nerve fiber bundles using optical coherence tomography with adaptive optics

Omer P. Kocaoglu [a,*], Barry Cense [b], Ravi S. Jonnal [a], Qiang Wang [a], Sangyeol Lee [a], Weihua Gao [a], Donald T. Miller [a]

[a] School of Optometry, Indiana University, 800 E. Atwater Avenue, Bloomington, IN 47405, United States
[b] Center for Optical Research and Education, Utsunomiya University, 7-1-2 Yoto, Utsunomiya, Tochigi 321-8585, Japan

ARTICLE INFO

Article history:
Received 12 April 2011
Received in revised form 13 June 2011
Available online 22 June 2011

Keywords:
Retinal nerve fiber bundles
Adaptive optics
Optical coherence tomography

ABSTRACT

Early detection of axonal tissue loss in retinal nerve fiber layer (RNFL) is critical for effective treatment and management of diseases such as glaucoma. This study aims to evaluate the capability of ultra-high-resolution optical coherence tomography with adaptive optics (UHR-AO-OCT) for imaging the RNFL axonal bundles (RNFBs) with $3 \times 3 \times 3\ \mu m^3$ resolution in the eye. We used a research-grade UHR-AO-OCT system to acquire $3^\circ \times 3^\circ$ volumes in four normal subjects and one subject with an arcuate retinal nerve fiber layer defect ($n = 5$; 29–62 years). Cross section (B-scans) and *en face* (C-scan) slices extracted from the volumes were used to assess visibility and size distribution of individual RNFBs. In one subject, we reimaged the same RNFBs twice over a 7 month interval and compared bundle width and thickness between the two imaging sessions. Lastly we compared images of an arcuate RNFL defect acquired with UHR-AO-OCT and commercial OCT (Heidelberg Spectralis). Individual RNFBs were distinguishable in all subjects at 3° retinal eccentricity in both cross-sectional and *en face* views (width: 30–50 μm, thickness: 10–15 μm). At 6° retinal eccentricity, RNFBs were distinguishable in three of the five subjects in both views (width: 30–45 μm, thickness: 20–40 μm). Width and thickness RNFB measurements taken 7 months apart were strongly correlated ($p < 0.0005$). Mean difference and standard deviation of the differences between the two measurement sessions were -0.1 ± 4.0 μm (width) and 0.3 ± 1.5 μm (thickness). UHR-AO-OCT outperformed commercial OCT in terms of clarity of the microscopic retina. To our knowledge, these are the first measurements of RNFB cross section reported in the living human eye.

1. Introduction

Early detection of axonal tissue loss is critical for managing diseases that destroy the retinal nerve fiber layer (RNFL) such as glaucoma, a leading cause of blindness throughout the world. Axonal tissue loss in the RNFL has been reported to be one of the earliest detectable glaucomatous changes, preceding morphologic changes in the optic nerve head and visual field loss (Alencar et al., 2010; Sakamoto et al., 2010; Seong et al., 2010; Sommer, Miller, Pollack, Maumenee, & George, 1977; Sommer et al., 1991). Many imaging modalities have been used to analyze RNFL loss in glaucomatous eyes, including: fundus photography (Hoyt, Frisen, & Newman, 1973; Miller & George, 1978; Muramatsu et al., 2010; Quigley et al., 1993); scanning laser polarimetry (Choplin, Zhou, & Knighton, 2003; Greenfield, Knighton, & Huang, 2000; Horn et al., 2009; Medeiros et al., 2009; Monteiro & Moura, 2008; Sehi, Ume, Greenfield, & Advanced Imaging in Glaucoma Study Group, 2007); scanning laser ophthalmoscopy (Alencar et al., 2010; Bowd et al., 2006; Caprioli, Park, Ugurlu, & Hoffman, 1998); and optical coherence tomography (OCT) (Budenz, Chang, Huang, Knighton, & Tielsch, 2005; Costa-Cunha, Cunha, Malta, & Monteiro, 2009; Harwerth, Wheat, & Rangaswamy, 2008; Horn et al., 2009; Kim, Park, Park, & Kim, 2007; Lu et al., 2008; Sakamoto et al., 2010; Seong et al., 2010). Fundus photography and scanning laser ophthalmoscope rely on local variations in fundus brightness (arcuate defects) to infer RNFL loss. Scanning laser polarimetry and OCT on the other hand measure local variations in RNFL phase retardation or thickness to infer RNFL loss, and polarization sensitive OCT measures both : (Cense, Chen, Park, Pierce, & de Boer, 2004, Gotzinger, Pircher, & Hitzenberger, 2005, Elmaanaoui et al., 2011). Regardless of method, however, none have the necessary lateral and axial resolution to image the 2D cross section of individual retinal nerve fiber bundles (RNFBs) as they traverse the retinal surface. Such imaging would be able to assess the thickness and width of individual RNFBs, and to differentiate RNFBs from the radial fibers of Müller cells that separate the bundles. This additional information

* Corresponding author. Fax: +1 812 855 7045.
E-mail addresses: okocaogl@indiana.edu (O.P. Kocaoglu), bcense@cc.utsunomiya-u.ac.jp (B. Cense), rjonnal@indiana.edu (R.S. Jonnal), wangqi@indiana.edu (Q. Wang), lee576@indiana.edu (S. Lee), wgao@indiana.edu (W. Gao), dtmiller@indiana.edu (D.T. Miller).

0042-6989/$ - see front matter © 2011 Elsevier Ltd. All rights reserved.
doi:10.1016/j.visres.2011.06.013

at the microscopic level opens the possibility to extend known morphological differences in RNFL thickness between normal, aging, and diseased retinal axonal tissue to morphological differences in RNFB cross-sectional area and volume.

More recently, images of individual RNFBs have been reported, acquired with retinal imaging systems equipped with adaptive optics (AO). AO increases imaging resolution and sensitivity, both of which are advantageous for detecting and differentiating the tightly packed RNFBs. AO scanning laser ophthalmoscopes (AO-SLOs) have successfully imaged RNFBs *en-face* (Burns, Tumbar, Elsner, Ferguson, & Hammer, 2007; Romero-Borja, Venkateswaran, Roorda, & Hebert, 2005; Roorda et al., 2002). AO has also been incorporated into optical coherence tomography (OCT) (Bigelow et al., 2007; Cense, Gao, et al., 2009; Cense, Koperda, et al., 2009; Fernandez et al., 2008; Hermann et al., 2004; Merino, Dainty, Bradu, & Podoleanu, 2006; Miller, Qu, Jonnal, & Thorn, 2003; Torti et al., 2009; Zawadzki, Choi, Jones, Oliver, & Werner, 2007; Zawadzki et al., 2005, 2008, 2009; Zhang, Rha, Jonnal, & Miller, 2005; Zhang et al., 2006). The major advantage of OCT is its substantially higher axial resolution (3–8 μm compared to >60 μm for AO-SLO and AO flood illumination retina cameras) which, when combined with AO, permits mapping of RNFBs in all three dimensions.

There have been several observational reports of AO-OCT imaging of individual RNFBs (Cense, Koperda, et al., 2009; Torti et al., 2009; Zawadzki et al., 2008). The 3D detail of the RNFBs reported with these instruments is impressive, but they are limited to single images acquired on single subjects with no measurements of the RNFB cross section. To establish grounds for a population study of RNFBs, this paper assesses the ability to image and measure the dimensions of RNFBs in four clinically normal subjects and one with an arcuate RNFL defect ($n = 5$; 29–62 years of age) at the same retinal eccentricities using the same UHR-AO-OCT instrument. $3^\circ \times 3^\circ$ volumes were acquired at three principal locations of the retina (3° nasal and 6° superior and inferior retinal eccentricity). Vertical and *en face* sections (B-scans and C-scans, respectively) extracted from the volumes were used for several kinds of analysis: to assess visibility and size distribution of individual RNFBs (five subjects); to assess ability to reimage the same RNFBs and to re-measure their size after 7 months (one subject); and to compare image quality of UHR-AO-OCT to that of commercial SD-OCT (one subject).

2. Materials and methods

The research-grade UHR-AO-OCT system used for this study is described in detail elsewhere (Cense, Koperda, et al., 2009; Zhang et al., 2006). In brief, the system is a fiber-based, low-coherence interferometer that includes a woofer–tweeter AO system and two spectrally broadband (>100 nm) light sources. The combination of AO and UHR-OCT achieves a 3D resolution of $3 \times 3 \times 3\ \mu m^3$ in retinal tissue. The woofer–tweeter AO, located in the sample arm, corrects monochromatic aberrations across the eye's dilated, 6 mm pupil, as well as aberrations generated by the system. The AO cascades an AOptix deformable mirror (DM) (37 electrodes; 16 μm stroke available for defocus) for correction primarily of lower-order aberrations and a Boston MicroMachines Corporation (BMC) DM (140 actuators; 3.8 μm stroke) for correction primarily of higher-order aberrations. Wavefront measurements are obtained with a Shack–Hartmann wavefront sensor (20×20 lenslet array). Correction of chromatic aberrations of the eye is realized with a customized achromatizing lens (Zawadzki et al., 2008).

The two light sources are a superluminescent diode (BroadLighter from Superlum Diodes Ltd., Moscow, Russia) with 110 nm bandwidth, center wavelength 840 nm, and output power 12 mW, and a Femtolasers Integral with 135 nm bandwidth, center wavelength at 800 nm and output power 60 mW. Analysis of the UHR-AO-OCT system in Cense, Koperda, et al. (2009) demonstrated approximately 3 μm axial resolution in retinal tissue with both light sources. A 14 μm, 2048-pixel linescan detector (E2 V, Chelmsford, England) in the detection arm captured the spectrum at a rate of 22.5 K lines/s. For the current study, the OCT control and acquisition software was upgraded to a 64-bit platform and recoded in C# and C++ for increased volume acquisition and storage, faster processing, and enhanced user control.

AO operation entailed sequential control of the AOptix and BMC DMs. Best correction of the AOptix DM was determined first, then the BMC DM. Once a stable maximum Strehl ratio was reached (typically >0.8 as measured by the wavefront sensor), dynamic AO with the BMC mirror continued at 22.5 Hz, during which OCT images of the retina were acquired. The large stroke of the AOptix mirror was also used to position system focus at the RNFL. Coarse adjustment in focus was guided by image quality of the UHR-AO-OCT image displayed in real time on the computer monitor. Fine adjustment of focus entailed acquiring a series of UHR-AO-OCT images of the same patch of retina with slightly different focus (typically ±0.05 Diopters) to ensure that clear images of RNFBs were obtained. This two-step focus procedure (coarse and fine) minimized the impact of focus error on the clarity of individual RNBs, the retinal layer of interest in this study. To illustrate the importance of proper focus, Fig. 1 shows two UHR-AO-OCT B-scans of essentially the same patch of retina, but with focus shifted by 0.4 D. The left B-scan shows that placement of focus at the photoreceptor layer is sufficient to prevent distinguishing individual RNFBs.

Four clinically normal subjects free of ocular disease (S1: 29-year old female, S2: 30-year old male, S3: 36-year old male, S4: 54-year old male) and one with an arcuate RNFL defect (S5: 62-year old male) were recruited. The RNFL defect accompanied the formation of a cotton wool spot of uncertain etiology. The chronology of the defect is described in detail by Chui, Thibos, Bradley and Burns (2009). Sphere and cylinder refractive errors ranged from 1 to 4.5 D and 0 to 1.25 D, respectively. All procedures on the subjects strictly adhered to the tenets of Helsinki declaration and the Institutional Review Board of Indiana University, and informed consent was obtained from all subjects. The maximum power delivered to the eye was 400 μW and 525 μW for Broadlighter and Integral light sources, respectively. Both power levels were within the A.N.S.I. standard (A.N.S.I., 2007). Eyes were dilated and cycloplegia maintained with hourly drops of 0.5% Tropicamide. A headrest and a bite bar were used to stabilize the subject's head, and a self-illuminated visual target provided fixation to the same eye that was imaged.

We acquired UHR-AO-OCT volumes of $3^\circ \times 3^\circ$ (900×900 μm) retinal patches with focus optimized (two-step focus procedure) for the RNFL. Because of practical constraints on the duration of the imaging sessions and the large data size of the volumes, we confined imaging in the normal subjects to three locations: retinal eccentricities of 6° superior and inferior to the fovea, and 3° nasal to the fovea. The 6° locations are reasonably representative of much of the RNFL across the retina, being 50 μm or less in thickness and consisting of a monolayer of RNFBs (Varma, Skaf, & Barron, 1996). The 3° location complements the 6° location, being noticeably thinner and containing the papillomacular bundles that are responsible for central vision. For the subject with the arcuate RNFL defect (S5), images were acquired that encompassed the width of the defect including the region 4.5° superior of the fovea, which is near to the 6° location imaged in the normal eyes.

The $3^\circ \times 3^\circ$ volumes consisted of 100 (fast) B-scans of 1000 A-scans each, and were acquired in 4.4 s. A-scan and B-scan spacing were 0.9 μm and 9 μm, respectively. B-scan spacing was purposefully coarser (10×), to enable rapid acquisition of large volumes

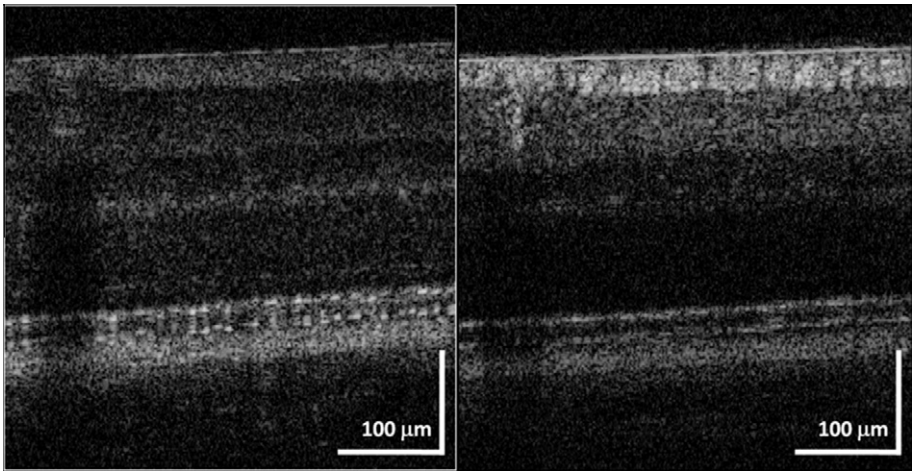

Fig. 1. Comparison of UHR-AO-OCT B-scans acquired of the same retinal location with AO focus at the photoreceptor layer (PL) (left) and RNFL (right). The 0.4 D shift in focus was generated by the AOptix mirror.

and reduce the impact of eye motion and tear film artifacts. Fast B-scans were oriented vertically on the retina so as to transect the RNFBs at all locations. This strategy helped preserve cross-sectional information of RNFBs across adjacent B-scans, thus permitting the averaging of successive B-scans to reduce speckle contrast with minimal loss in RNFB detail. At the 6° locations, effective averaging required the use of oblique B-scans, realized by interpolation of the volume in post processing.

Axial eye motion artifacts were removed from the UHR-AO-OCT volumes using custom software developed in our laboratory (ImageJ plugin). This entailed axially shifting fast B-scans to align the connecting cilia reflection of the photoreceptors. We used an additional custom plugin to extract B-scans (fast and oblique) and C-scans of the RNFL, and a volume renderer, developed at the Institute for Data Analysis and Visualization (IDAV) of the University of California at Davis, to view volumes (Fuller et al., 2007). A log-intensity scale was used to display all AO-OCT images and videos. We also recorded wide-field (30° × 30°) SLO images of the same eyes using Heidelberg Engineering Spectralis (Vista, CA) that confirmed the actual retinal location of the UHR-AO-OCT volumes. This entailed projecting the UHR-AO-OCT volumes onto the wide-field SLO images and then manually registering (*xy*) to determine the location of overlap. The distinct vasculature, evident in both images, helped facilitate the process. We assessed visibility of individual RNFBs in the B-scans and C-scans. We also measured the cross-sectional dimensions (width × thickness) of RNFBs in averaged B-scans for the five subjects and three retinal locations imaged. For each subject and retinal location, approximately 10 bundles were manually selected and measured. Bundles were selected randomly, but needed to be distinguishable from neighboring bundles to allow measurement. Width and thickness measurements were made on the widest and thickest part of the selected bundles, respectively. Measurements in this way were not affected by differences in the internal appearance of the bundles and insensitive to micro-variations of the bundle contours, as for example from speckle noise.

For one subject, we repeated imaging of the same RNFB patch 7 months after the first imaging session to demonstrate the feasibility of returning to and measuring the same bundles. We assessed the repeatability of width and thickness measurements of RNFBs between the two sessions. Finally, we compared UHR-AO-OCT to commercial OCT (Spectralis) images acquired in the same subject (S5). Comparison was made in terms of visibility of the microscopic retinal structure and 2D speckle size.

3. Results

3.1. RNFB visibility and size distribution in cross section

Fig. 2 shows a representative UHR-AO-OCT volume obtained at 6° superior in one of the four normal subjects (S1). The uppermost retinal surface in the corresponding video – which we interpret to be the inner limiting membrane (ILM) – was removed in postprocessing to reveal the corrugated pattern of the underlying RNFL, composed of brightly reflecting bands separated by thin, dark gaps. The video (Video 1) that accompanies the figure examines the bands – which we interpret here to be individual axonal RNFBs – from several points of view, realized by rotating and sectioning the volume in several steps to show top, bottom, and cross-sectional views of the bundles. The retinal location of the volume was confirmed by projecting it onto the wide-field SLO image, acquired on the same subject. For another subject (S4), Fig. 3A shows the locations of the UHR-AO-OCT

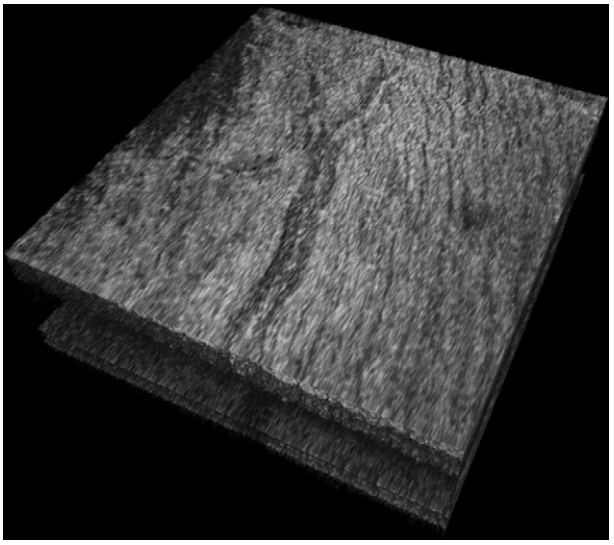

Fig. 2. Movie showing a 3° × 3° UHR-AO-OCT volume acquired at 6° superior to the fovea in one subject (S1). Focus is at the RNFL. Video 1 highlights the three dimensional structure of individual RNFBs. The video was generated using the volume renderer by IDAV.

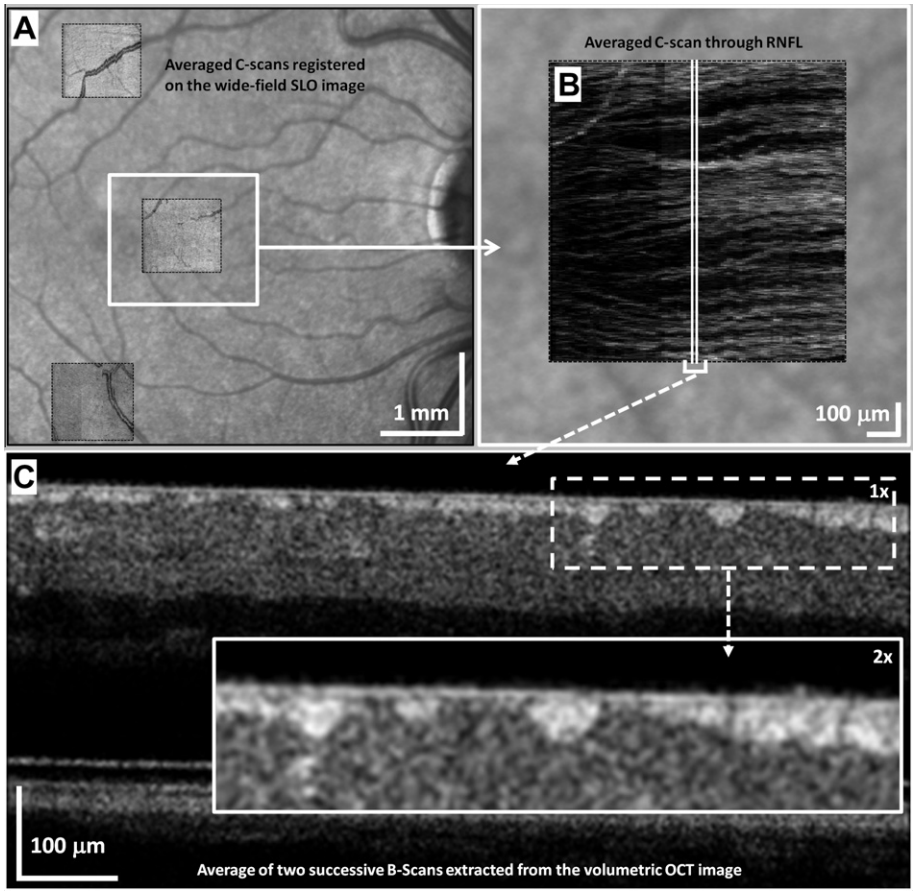

Fig. 3. (A) Projections of the UHR-AO-OCT volumes onto the wide-field SLO image of subject S4. Alignment of the projections to the SLO image confirms the 3° (nasal) and 6° (superior and inferior) retinal locations from the fovea. (B) Averaged C-scan through the RNFL reveals individual RNFBs that traverse from the optic disc to fovea (right to left). Note that to fully capture the RNFBs over the 3° field, C-scans were averaged over a 30 μm thick section that was slightly tilted (in post processing) to coarsely approximate the retinal curvature. (C) Average of two successive B-scans taken from the 3° *en-face* image (white lines) reduces speckle contrast and improves bundle clarity. Note that left edge of the B-scan corresponds to bottom edge of *en*-face image. Video 2 highlights the 3D appearance of the isolated RNFL. Video 3 shows a cross-sectional fly through of the entire UHR-AO-OCT volume.

volumes collected at 6° superior, 6° inferior, and 3° nasal. Good agreement was found between expected and confirmed locations of the volumes.

Fig. 3B and C shows enlarged *en-face* and cross-sectional views of the volume at 3° nasal, again on subject S4. The *en-face* view consists of an averaged C-scan slice through just the RNFL. Individual bundles are clearly distinguishable in the slice, traversing the image from optic disc to fovea (right to left). The bundles reflect noticeably more light than the surrounding tissue, a factor of approximately two times more. As they approach the fovea, the RNFBs thin (both in width and depth) and separate. These features are more readily apparent in the accompanying videos (Videos 2 and 3), which capture the entire breadth of the RNFBs as they follow the topography of the retina near the foveal pit. Over much of the volume, the RNFBs share the same orientation, and this enables averaging of adjacent B-scans (which are orthogonal to the bundle direction) to reduce speckle noise without sacrificing spatial information of the RNFB cross section (width and thickness). An example is given in Fig. 3C that shows an average of two successive B-scans, denoted by the parallel white lines in the center of the *en-face* image.

Next we measured the cross-sectional dimensions of individual RNFBs. Fig. 4 plots the measurements (width and thickness) for the two retinal eccentricities (3° and 6°) and five subjects, including the subject with the arcuate defect. Note that for 6°, measurements were obtained only for three subjects. Individual RNFBs could not be distinguished for the other two owing to the bundles' tighter packing and correspondingly narrower gaps.

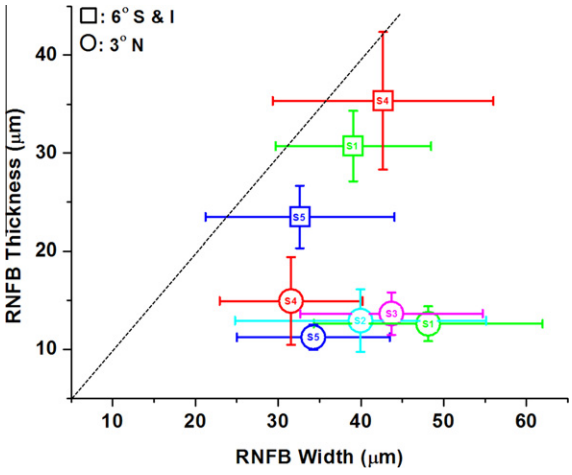

Fig. 4. Average width and thickness of RNFBs measured at 3° nasal (N) and 6° superior (S) and inferior (I) retinal eccentricities for five subjects. Error bars represent the distribution of RNFB sizes measured at each retinal eccentricity, defined as the standard deviation of 10 separate RNFBs at that location. For reference, the dashed line denotes a perfectly circular bundle (width = thickness). S5 is the subject with arcuate RNFL defect.

3.2. Seven-month repeatability of RNFB size in one subject

UHR-AO-OCT volumes were acquired in separate imaging sessions administered 7 months apart on subject S1. Volumes were acquired at 6° superior to the fovea. Fig. 5A shows the registration of the UHR-AO-OCT projections to each other and to the wide-field SLO image. As evident in Fig. 5B_1 and B_2, the projections overlap substantially with a lateral displacement less than 100 μm. Because the striate pattern of the RNFBs is not perpendicular to the fast B-scan direction (which is vertical in the C-scans), direct averaging of successive B-scans to enhance bundle clarity yielded unacceptable blur. To circumvent this problem, we manually chose an orientation perpendicular to the bundles and interpolated oblique B-scans in that orientation, as indicated in Fig. 5 by the solid and dashed lines superimposed on the C-scans. Fig. 5C_1 and C_2 shows the corresponding interpolated oblique B-scans. Width and thickness dimensions of the RNFBs in the figure correspond approximately to the 6° data of subject S1 in Fig. 4.

For unknown reasons, clarity of individual bundles was reduced in the second session, yet still sufficient to reveal similar bundle features and shapes found in the first B-scan (compare Fig. 5C_1 and C_2). To quantify the extent of these similarities and to determine potential sources of error that may limit such comparisons (e.g., differences in image magnification, resolution, and dynamic range), width and thickness measurements were made on bundles identified in both imaging sessions. Measurements ($n = 10$) were plotted against each other (session 1 versus session 2), and a least squares regression fit showed a high correlation for both width ($y = -0.650 + 1.022x$, $R^2 = 0.874$, $p < 0.0005$) and thickness ($y = -0.934 + 1.020x$, $R^2 = 0.768$, $p < 0.0005$) measurements. To test for agreement, absolute differences between repeat measurements on the same bundles were plotted against their mean following the Bland–Altman method (Altman and Bland, 1983). Fig. 6 shows the resulting comparison with measurements of width on the left and thickness on the right. The absolute difference mean and standard deviation were −0.1 μm and 4.0 μm, respectively for bundle width, and 0.3 μm and 1.5 μm for bundle thickness.

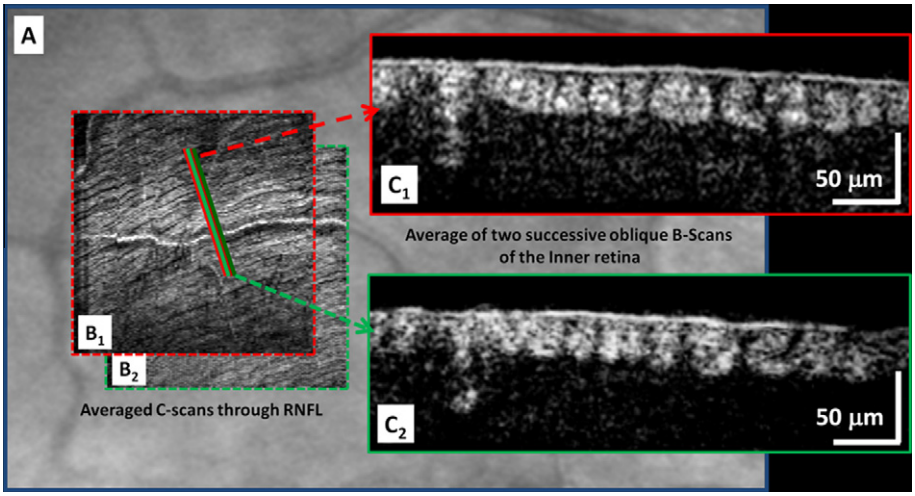

Fig. 5. UHR-AO-OCT images acquired 7 months apart on the same subject (S1) (A) Wide-field SLO image facilitated registration of the projected C-scans. (B_1 and B_2) C-scans averaged through the RNFL reveal the diagonal striation pattern of RNFBs and the presence of retinal vasculature. Solid lines denote the first imaging session (acquired with Integral light source), dashed lines the second (acquired with Broadlighter light source). (C_1 and C_2) Averaged (2), oblique B-scans of the same retinal location.

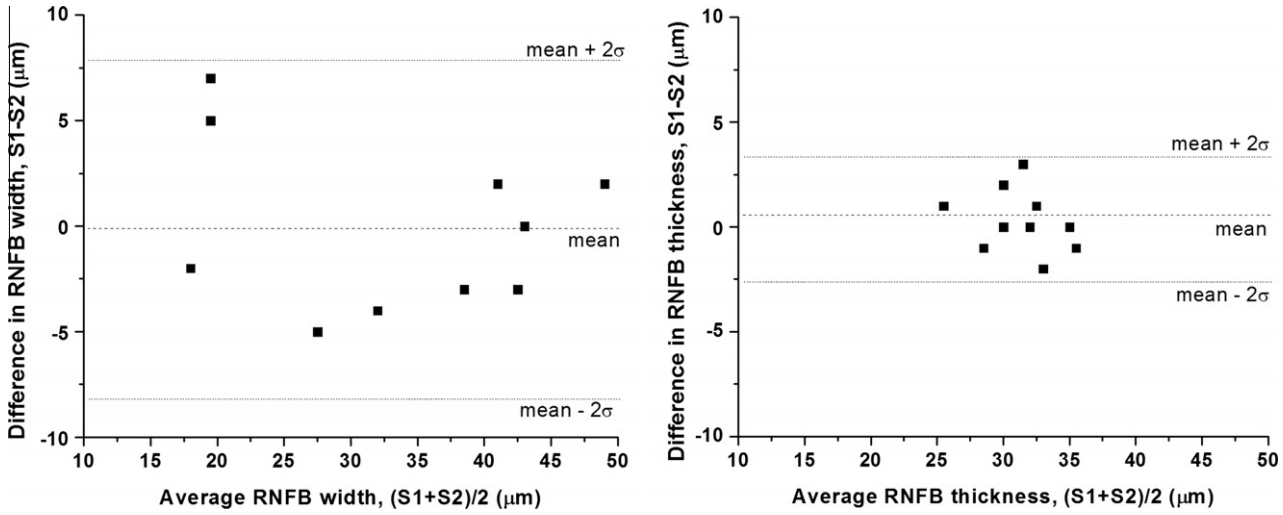

Fig. 6. Bland–Altman plots showing difference against mean for width (left) and thickness (right) measurements of the two imaging sessions, S1 and S2. Dashed and dotted lines indicate the mean difference and 95% confidence intervals (±2 standard deviations of the mean differences), respectively.

3.3. Arcuate RNFL defect imaging and comparison with commercial SD-OCT

The arcuate RNFL defect of subject S5 appears as a slightly darkened strip (~250 μm wide) on the wide-field SLO image, suggestive of RNFL thinning. Arrows in Fig. 7A mark the location of the defect, which begins near the optic disc and extends into the superior retina. To assess the ability of UHR-AO-OCT to image this defect, 3° × 3° volumes were acquired at several locations along the defect as shown in Fig. 7A. Fig. 7B shows a C-scan projection of one such volume that encompasses the width of the defect at about 4.5° superior of the fovea. The darkened strip visible in the C-scan is consistent with that in the SLO image in terms of location and size. In Fig. 7C, oblique B-scans perpendicular to the RNFB direction (white lines in Fig. 7B) confirm substantial loss of the RNFL in the defect area along with a possible thickening of the underlying outer neural layers. In Fig. 7C, thickness of the RNFL is reduced from 40 μm (adjacent to the defect) to 10 μm (within the defect). Individual RNFBs could not be distinguished in the defect even though the RNFL was exceedingly thin there and perpendicular to the oblique B-scans. RNFBs were also not distinguishable in the neighboring regions.

Spectralis OCT B-scans were also collected of the arcuate RNFL defect, an example of which is shown in Fig. 8A. Fig. 8B shows a corresponding UHR-AO-OCT B-scan of essentially the same patch of retina. Unlike the oblique B-scan in Fig. 7, which required interpolating between fast B-scans spaced 9 μm apart, Fig. 8B is an average of 7 fast B-scans (vertical with 0.9 μm spacing). The averaging is consistent with the default averaging mode of the Spectralis system, for a fairer comparison. To assess differences in speckle size (axial and lateral) between the Spectralis and UHR-AO-OCT images, an autocorrelation was computed for the small areas enclosed by the boxes of Fig. 8A and B. These regions were chosen for their uniform homogeneity, lacking apparent structures with sharp edges such as vessels and boundaries between neural layers, which can influence the correlation. Results of the

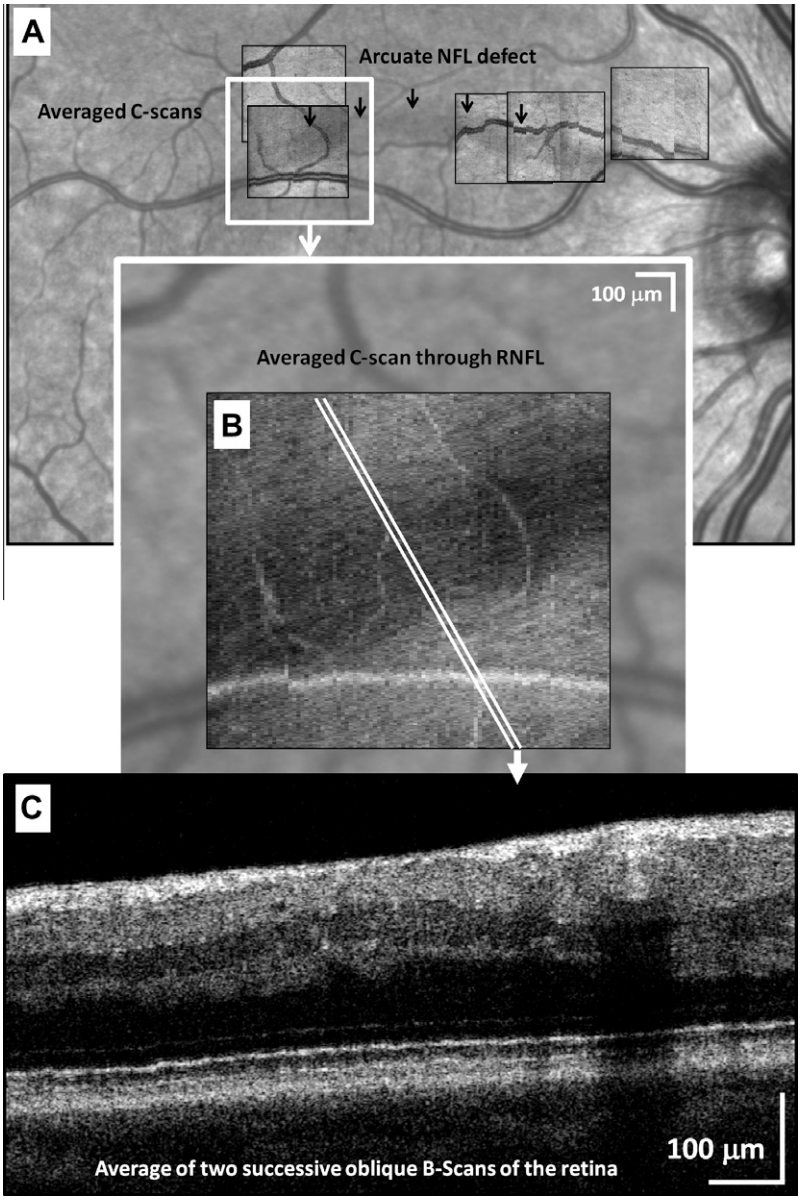

Fig. 7. UHR-AO-OCT images of the arcuate RNFL defect in subject #5. (A) UHR-AO-OCT volumes are laterally registered to the wide-field SLO image using projection C-scans. (B) Enlarged view of a C-scan averaged through the RNFL. (C) B-scan obtained by averaging two successive oblique B-scans that are approximately perpendicular to the RNFB direction.

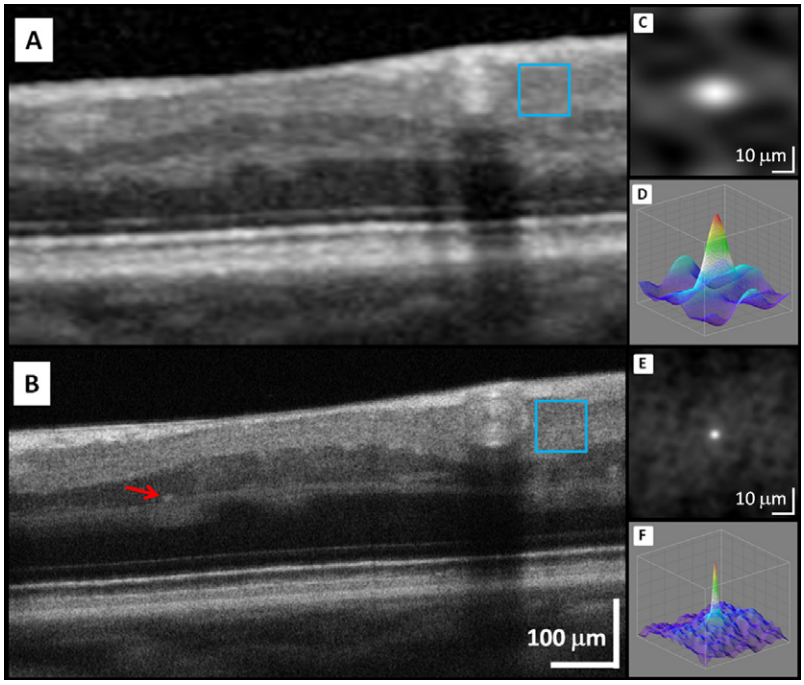

Fig. 8. Comparison of fast B-scans acquired of the same patch of retina with the (A) Heidelberg Spectralis and (B) UHR-AO-OCT instrument. B-scans were obtained on subject S5 at 4.5° superior to the fovea, a section that crossed the arcuate RNFL defect. Arrow points to a retinal capillary that becomes more evident compared to (A). (C and E) show the autocorrelation (gray scale map) for the region inside the superimposed box in (A and B), respectively. Surface plots of the autocorrelation maps are shown in (D) and (F).

correlation are shown in Fig. 8C and D (Spectralis) and E and F (UHR-AO-OCT), both depicted on a linear intensity scale. The full width at half maximum (FWHM) of the autocorrelation peak, which corresponds to the average speckle size, was measured to be 7.32 μm × 11.42 μm (axial × lateral) and 2.85 μm × 3.03 μm for the Spectralis and UHR-AO-OCT, respectively.

4. Discussion

In this study we investigated the capability of UHR-AO-OCT to image individual RNFBs as captured in 3° × 3° volume datasets on five subjects. Most volumes were acquired at retinal eccentricities of 3° nasal and 6° superior and inferior. Cross-sectional (B-scans) and *en face* (C-scan) views extracted from the volumes were used to assess visibility and size of individual RNFBs; to assess ability to reimage the same RNFBs and to re-measure their size after 7 months; and to compare image quality of UHR-AO-OCT to that of commercial SD-OCT.

4.1. RNFB visibility and size distribution in cross section

Clarity of individual bundles in both B-scan and C-scan views varied with subject and retinal location. These subject- and eccentricity-dependencies are not evident in the existing published AO-OCT studies of RNFBs. The overriding determinant of bundle clarity was size of the gap between adjacent bundles rather than the size of the bundles themselves. Spacing between adjacent bundles was on the order of a few microns compared to the size of bundles, which was on the order of tens of microns. The former is comparable to the resolution of the UHR-AO-OCT system ($3 \times 3 \times 3\ \mu m^3$). Gap size at 3° retinal eccentricity was found consistently larger than that at 6° enabling bundles to be more readily identified. RNFBs were distinguishable in all five subjects at 3° compared to three at 6°. Critical for identifying bundles is bundle contrast. The reflectance of RNFB tissue was found to be approximately two times brighter (3 dB) than that of the Müller cells that surround the bundles (gaps), regardless of the the 3° and 6° locations imaged. This difference provided sufficient contrast to easily distinguish bundle from gap when resolution allowed. It is worth noting, however, that reflectance of nerve fiber bundles is well known to be directional (Knighton & Huang, 1999; Knighton & Qian, 2000) and therefore its difference with the Müller cells may vary – perhaps significantly – with bundle orientation and illumination angle. This effect was not investigated.

While our study targeted the 3° and 6° retinal eccentricity locations, volumes were also collected close to the optic disc (within 1.7 mm superior and temporal of the optic disc center) on one of the subjects. A representative example is shown in Video 4. Close to the optic nerve head, the RNFL is known to become increasingly thick (e.g., 115 μm in Video 4) with bundles larger in size and more irregular in shape, and intermixed with large vessels. We were unable confidently to distinguish individual bundles at these thicker locations owing to the increased complexity of the RNFL. To distinguish bundles here may require additional or more clever methods of averaging of B-scans to enhance structure contrast (increase signal to noise; reduce speckle noise) and/or augmentation of intensity-based imaging with other forms of OCT imaging (Doppler OCT; Izatt, Kulkarni, Yazdanfar, Barton, & Welch, 2007; Wang, Bower, Izatt, Tan, & Huang, 2007 ; Leitgeb et al., 2003; Makita, Hong, Yamanari, Yatagai, & Yasuno, 2006) to help distinguish bundle from vessel.

We quantified the cross-sectional dimensions (width × thickness) of the RNFBs at 3° and 6° retinal eccentricity, the results of which are plotted in Fig. 4. The figure shows that regardless of subject and retinal eccentricity examined, bundles are almost always wider than they are thick. However, bundles at 3° demonstrate a larger aspect ratio (width to thickness) than those at 6° with average width and thickness ranging from 30 to 50 μm and 10 to 15 μm, respectively, across the five subjects examined. Bundles at 6° are of comparable width to the 3° bundles, but roughly two times thicker. The average width and thickness ranges from 30 to 45 μm and 20 to 40 μm, respectively, for the three subjects in which bundles could be identified.

Error bars in the Fig. 4 plot capture the distribution of bundle width and thickness at these two retinal eccentricities for each subject. The plot reveals a noticeably larger distribution in bundle width compared to bundle thickness. Specifically, the average standard deviation (error bar) of the bundle width for the eight data points in the figure is 11.5 μm, compared to 3.3 μm for the bundle thickness, a distribution difference of 3.5 times. Note that these relatively large variations in RNFB size even at the same retinal patch are not due to measurement error (which is tested in Fig. 6 and discussed below), but rather reflect differences in the anatomical structure of individual bundles. We found these bundle differences easy to detect with AO-OCT and facilitated identification of the same bundle for repeated measurements. Because of this, such differences may actually improve our ability to detect subtle bundle changes caused by retinal diseases as for example glaucoma.

The small number of subjects in this study precludes testing for subject differences. Nevertheless it is interesting to note that the smallest average RNFB widths (see Fig. 4) occurred in the two oldest subjects at 3° (S4 and S5) and the oldest subject at 6°. Not all subjects fit this trend, however, as for example the next older subject (S4) at 6° had the largest average width. Such width measurements may be helpful for understanding the effects of normal aging and glaucomatous neuropathy on axonal loss. For example, it is well established that axonal loss thins the RNFL, a process that can be measured with clinical OCT. However, the measured rate of thinning (~0.2%/year) is noticeably less than age-related loss of retinal ganglion cells (~0.6%/year) measured with perimetry. A leading hypothesis that attempts to reconcile this difference is that axonal loss triggers a remodeling of the RNFL that increases its non-neuronal content (Harwerth & Wheat, 2008; Harwerth et al., 2008). This increase partially offsets the axonal loss. While indirect evidence of this increase has been reported, the UHR-AO-OCT method presented here represents an alternative approach that in principle can directly separate the neuronal and non-neuronal contributions of the RNFL, at least in terms of the total cross sectional area of axonal bundles and that of the gaps between them.

4.2. Reimaging RNFBs after 7 month interval

We imaged twice the same RNFB patch at 6° retinal eccentricity in one subject with imaging sessions separated by 7 months. We found that the same RNFBs and effectively the same cross section of the bundles could be readily located (Fig. 5) and measured (Fig. 6). Strong correlation was found for repeated measurements of width ($R^2 = 0.874$) and thickness ($R^2 = 0.768$) with both being statistically significant ($p < 0.0005$). Repeatability of width and thickness demonstrated a regression slope showing only 2.0% and 2.2% deviations respectively (proportional systematic error) from the ideal $Y = X$ lines. The Bland–Altman plot in Fig. 6 depicts a test for measurement agreement. The absolute difference mean and standard deviation were −0.1 μm and 4.0 μm, respectively for bundle width, and 0.3 μm and 1.5 μm for bundle thickness. The small mean differences are a fraction of a micron (−0.1 μm and 0.3 μm) and suggest system-related errors (biases), such as slight differences in lateral magnification or resolution, are negligible. It also includes errors associated with system axial magnification, axial resolution, and dispersion compensation that would affect thickness measurements.

As shown in the plot, all difference measurements fall within the 95% confidence limits (±2 standard deviations) that correspond to ±8.0 μm (width) and ±3.0 μm (thickness). While the thickness measurements demonstrate approximately 2.5 times better agreement than the width measurements, much of the width disagreement occurs for the narrower RNFBs. For example the 95% confidence limit for the narrower half (<33.5 μm) is ±10.7 μm compared to ±4.9 μm for the wider half (>33.5 μm). It is unclear why narrower RNFBs were more difficult to repeatedly measure. Blur caused by the optical resolution of the UHR-AO-OCT may be the root of this difference, albeit unlikely. The optical resolution was essentially the same in all dimensions ($3 \times 3 \times 3\ \mu m^3$), which leads to a homogeneous blur, and noticeably less than the measured ±8.0 μm (width) confidence limit. Furthermore, the optical performance of the UHR-AO-OCT system as reported by the SHWS was stable during the volume acquisitions, indicating that the same amount of blur was applied to the RNFBs regardless of their location in the 3° field.

Another possible cause is eye motion artifacts, which can affect width measurements more than thickness measurements. Width measurements rely on volume pixels acquired as much as 40 ms apart (extracted from different B-scans), whereas thickness measurements rely on volume pixels of the same A-scan, and thus acquired simultaneously. The much longer time interval needed for the width measurements exposes them to increased motion artifacts. The same line of reasoning, however, also means that larger RNFBs should be more prone to measurement error than smaller ones as the former requires more B-scans to sample the bundle cross section. However, Fig. 6 shows the opposite trend (agreement increases with RNFB size), thus providing strong evidence that eye motion likely plays a minor role.

Perhaps the most likely cause of reduced agreement for narrower RNFBs is the uneven sampling of the volume images at $0.9 \times 9 \times 1\ \mu m^3$, which corresponds to 0.9 μm A-scan spacing, 9 μm B-scan spacing, and 1 μm depth spacing. While all thickness measurements were based on 1 μm depth sampling, width measurements required interpolation of the RNFBs between the finely spaced (0.9 μm) A-scans and coarsely spaced (9 μm) B-scans. Interpolation was necessitated by the oblique orientation of the RNFBs relative to the fast B-scans (see Fig. 5). While not obvious from the cross sections, faithful reconstruction of the narrow RNFBs may have been more sensitive to this non-linear operation than that of the wider ones and furthermore more sensitive to the actual sample locations, which would have been different for the two imaging sessions. Of course sampling the retina ten times finer with B-scans (0.9 μm instead of 9 μm) would directly test this hypothesis; this, however, would increase acquisition time by a factor of 10 as well, from 4.4 s to 44 s, which is not practical. This time difference could be partially offset by use of a higher speed linescan camera in the detection channel of the UHR-AO-OCT for increased image acquisition. Such high speed acquisition has already been demonstrated for imaging and tracking individual cone photoreceptors (Kocaoglu et al., 2011). This remains future work.

While technical issues remain as how best to optimize the repeatability of the width measurements and to a lesser extent the thickness measurements, the results demonstrate successful use of UHR-AO-OCT to locate the same bundles and to measure bundle cross section. The 7 month interval between imaging sessions approaches the annual time frame used to monitor glaucoma progression in patients. The comparable time interval provides encouragement that such an instrument could be used in longitudinal studies of this disease.

4.3. Comparison of UHR-AO-OCT with commercial SD-OCT

We previously quantified the benefit of adding AO to a research-grade high-resolution SD-OCT instrument in terms of signal-to-noise, lateral resolution, and speckle size (Cense, Gao, et al., 2009). Significant improvement in all three areas was observed and attributable to the use of a larger pupil (6 mm compared to 1.2 mm) afforded by AO. Here we considered a similar comparison, this time between UHR-AO-OCT (representing an improved version of the system in Cense, Gao, et al., 2009) and state-of-the-art commercial SD-OCT (Spectralis). Both instruments ac-

quired B-scans of essentially the same patch of retina (see Fig. 8). As clear from the figure, the most striking benefit of UHR-AO-OCT comes from the much smaller speckle size, measured at 2.9 μm × 3.0 μm (axial × lateral) compared to 7.3 μm × 11.4 μm for the Spectralis. Based on these numbers, the speckle area of the UHR-AO-OCT is substantially smaller (9.6 times smaller) than that of the Spectralis, and not surprisingly makes a striking improvement in visual clarity of the microscopic retina. Note that this smaller speckle size is not confined to the depth of focus (as is lateral resolution), which was placed in this example in the RNFL, but instead extends over the entire depth of the retina. As evident in Fig 8A and B, boundaries between the neural interfaces are sharper in the UHR-AO-OCT B-scan compared to the Spectralis, the side walls (inner and outer) of the major blood vessel become visible, retinal capillaries are more evident (see the arrow), and the outer retinal layers (in particular the PL and RPE) are better defined. In general, UHR-AO-OCT provides superior visibility of the microscopic retina compared to the Spectralis SD-OCT.

5. Conclusion

Results of this paper demonstrate that UHR-AO-OCT is readily capable of measuring the cross sectional profile of individual bundles, even at locations where they are increasingly thin (<15 μm) and packed closely together. We know of no other imaging modality capable of imaging RNFBs at this level. Furthermore, UHR-AO-OCT permits repeated measurements of the same individual RNFBs for imaging sessions separated by months. While the UHR-AO-OCT results presented here are encouraging, quality of the RNFB images will inevitably improve with further advances in the underlying AO and OCT technologies. For example, the recent availability of ultra-high-speed line-scan cameras opens the possibility to substantially reduce eye-motion artifacts and increase sampling density of the retina. Both will increase our ability to individuate RNFBs and our precision to measure their areal cross section and volume.

Acknowledgments

We gratefully acknowledge the contributions of Robert Zawadzki and John Werner (Department of Ophthalmology and Vision Science, University of California at Davis), and Steven Jones and Scot Olivier (Lawrence Livermore National Laboratory). We thank Alfred R. Fuller, David F. Wiley, and Bernd Hamann (IDAV, University of California at Davis) for use of their volume renderer software. We thank Bill Swanson for suggestions on the 7-month study, Toco Chui for taking the SLO images, and Thomas Kemerly, Daniel Jackson, and William Monette for machining and electronic support. Financial support was provided by the National Eye Institute Grants 5R01 EY014743, 1R01 EY018339, and P30 EY019008.

Appendix A. Supplementary material

Supplementary data associated with this article can be found, in the online version, at doi:10.1016/j.visres.2011.06.013.

References

A.N.S.I. (2007). *Z136.1 Safe use of lasers*. Laser Institute of America.

Alencar, L. M., Zangwill, L. M., Weinreb, R. N., Bowd, C., Sample, P. A., Girkin, C. A., et al. (2010). A comparison of rates of change in neuroretinal rim area and retinal nerve fiber layer thickness in progressive glaucoma. *Investigative Ophthalmology and Visual Science, 51*, 3531–3539.

Altman, D. G., & Bland, J. M. (1983). Measurement in medicine: The analysis of method comparison studies. *The Statistician, 32*, 307–317.

Bigelow, C. E., Iftimia, N. V., Ferguson, R. D., Ustun, T. E., Bloom, B., & Hammer, D. X. (2007). Compact multimodal adaptive-optics spectral-domain optical coherence tomography instrument for retinal imaging. *Journal of the Optical Society of America A – Optics and Image Science, 24*, 1327–1336.

Bowd, C., Zangwill, L. M., Medeiros, F. A., Tavares, I. M., Hoffmann, E. M., Bourne, R. R., et al. (2006). Structure–function relationships using confocal scanning laser ophthalmoscopy, optical coherence tomography, and scanning laser polarimetry. *Investigative Ophthalmology and Visual Science, 47*, 2889–2895.

Budenz, D. L., Chang, R. T., Huang, X., Knighton, R. W., & Tielsch, J. M. (2005). Reproducibility of retinal nerve fiber thickness measurements using the stratus OCT in normal and glaucomatous eyes. *Investigative Ophthalmology and Visual Science, 46*, 2440–2443.

Burns, S. A., Tumbar, R., Elsner, A. E., Ferguson, D., & Hammer, D. X. (2007). Large-field-of-view, modular, stabilized, adaptive-optics-based scanning laser ophthalmoscope. *Journal of the Optical Society of America A – Optics Image Science and Vision, 24*, 1313–1326.

Caprioli, J., Park, H. J., Ugurlu, S., & Hoffman, D. (1998). Slope of the peripapillary nerve fiber layer surface in glaucoma. *Investigative Ophthalmology and Visual Science, 39*, 2321–2328.

Cense, B., Chen, T. C., Park, B. H., Pierce, M. C., & de Boer, J. F. (2004). *In vivo* birefringence and thickness measurements of the human retinal nerve fiber layer using polarization-sensitive optical coherence tomography. *Journal of Biomedical Optics, 9*, 121–125.

Cense, B., Gao, W., Brown, J. M., Jones, S. M., Jonnal, R. S., Mujat, M., et al. (2009). Retinal imaging with polarization-sensitive optical coherence tomography and adaptive optics. *Optics Express, 17*(24), 21634–21651.

Cense, B., Koperda, E., Brown, J. M., Kocaoglu, O. P., Gao, W., Jonnal, R. S., et al. (2009). Volumetric retinal imaging with ultrahigh-resolution spectral-domain optical coherence tomography and adaptive optics using two broadband light sources. *Optics Express, 17*(5), 4095–4111.

Choplin, N. T., Zhou, Q., & Knighton, R. W. (2003). Effect of individualized compensation for anterior segment birefringence on retinal nerve fiber layer assessments as determined by scanning laser polarimetry. *Ophthalmology, 110*(4), 719–725.

Chui, T. Y., Thibos, L. N., Bradley, A., & Burns, S. A. (2009). The mechanisms of vision loss associated with a cotton wool spot. *Vision Research, 49*(23), 2826–2834.

Costa-Cunha, L. V. F., Cunha, L. P., Malta, R. F. S., & Monteiro, M. L. R. (2009). Comparison of Fourier-domain and time-domain optical coherence tomography in the detection of band atrophy of the optic nerve. *American Journal of Ophthalmology, 147*(1), 56–63.

Elmaanaoui, B., Wang, B., Dwelle, J. C., McElroy, A. B., Liu, S. S., Rylander, H. G., et al. (2011). Birefringence measurement of the retinal nerve fiber layer by swept source polarization sensitive optical coherence tomography. *Optics Express, 19*, 10252–10268.

Fernandez, E. J., Hermann, B., Povazay, B., Unterhuber, A., Sattmann, H., Hofer, B., et al. (2008). Ultrahigh resolution optical coherence tomography and pancorrection for cellular imaging of the living human retina. *Optics Express, 16*, 11083–11094.

Fuller, A., Zawadzki, R., Choi, S., Wiley, D., Werner, J., & Hamann, B. (2007). Segmentation of three-dimensional retinal image data. In *IEEE transactions on visualization and computer graphics* (pp. 1719–1726).

Götzinger, E., Pircher, M., & Hitzenberger, C. K. (2005). High speed spectral domain polarization sensitive optical coherence tomography of the human retina. *Optics Express, 13*, 10217–10229.

Greenfield, D. S., Knighton, R. W., & Huang, X. R. (2000). Effect of corneal polarization axis on assessment of retinal nerve fiber layer thickness by scanning laser polarimetry. *American Journal of Ophthalmology, 129*(6), 715–722.

Harwerth, R. S., & Wheat, J. L. (2008). Modeling the effects of aging on retinal ganglion cell density and nerve fiber layer thickness. *Graefes Archive for Clinical and Experimental Ophthalmology, 246*, 305–314.

Harwerth, R. S., Wheat, J. L., & Rangaswamy, N. V. (2008). Age-related losses of retinal ganglion cells and axons. *Investigative Ophthalmology and Visual Science, 49*, 4437–4443.

Hermann, B., Fernández, E. J., Unterhuber, A., Sattmann, H., Fercher, A. F., Drexler, W., et al. (2004). Adaptive-optics ultrahigh-resolution optical coherence tomography. *Optics Letters, 29*, 2142–2144.

Horn, F. K., Mardin, C. Y., Laemmer, R., Baleanu, D., Juenemann, A. M., Kruse, F. E., et al. (2009). Correlation between local glaucomatous visual field defects and loss of nerve fiber layer thickness measured with polarimetry and spectral domain OCT. *Investigative Ophthalmology and Visual Science, 50*, 1971–1977.

Hoyt, W. F., Frisen, L., & Newman, N. M. (1973). Fundoscopy of nerve fiber layer defects in glaucoma. *Investigative Ophthalmology and Visual Science, 12*, 814–829.

Izatt, J. A., Kulkarni, M. D., Yazdanfar, S., Barton, J. K., & Welch, A. J. (2007). *In vivo* bidirectional color Doppler flow imaging of picoliter blood volumes using optical coherence tomography. *Optics Letters, 22*(18), 1439–1441.

Kim, T. W., Park, U. C., Park, K. H., & Kim, D. M. (2007). Ability of stratus OCT to identify localized retinal nerve fiber layer defects in patients with normal standard automated perimetry results. *Investigative Ophthalmology and Visual Science, 48*(4), 1635–1641.

Knighton, R. W., & Huang, X. R. (1999). Directional and spectral reflectance of the rat retinal nerve fiber layer. *Investigative Ophthalmology and Visual Science, 40*(3), 639–647.

Knighton, R. W., & Qian, C. (2000). An optical model of the human retinal nerve fiber layer: Implications of directional reflectance for variability of clinical measurements. *Journal of Glaucoma, 9*(1), 56–62.

Kocaoglu, O. P., Lee, S., Jonnal, R. S., Wang, Q., Herde, A. E., Derby, J. C., et al. (2011). Imaging cone photoreceptors in three dimensions and in time using ultrahigh resolution optical coherence tomography with adaptive optics. *Biomedical Optics Express, 2*(4), 748–763.

Leitgeb, R., Schmetterer, L., Drexler, W., Fercher, A., Zawadzki, R., & Bajraszewski, T. (2003). Real-time assessment of retinal blood flow with ultrafast acquisition by color Doppler Fourier domain optical coherence tomography. *Optics Express, 11*, 3116–3121.

Lu, A. T. H., Wang, M. W., Verma, R., Schuman, J. S., Greenfield, D. S., Smith, S. D., et al. (2008). Combining nerve fiber layer parameters to optimize glaucoma diagnosis with optical coherence tomography. *Ophthalmology, 115*(8), 1352–1357.

Makita, S., Hong, Y., Yamanari, M., Yatagai, T., & Yasuno, Y. (2006). Optical coherence angiography. *Optics Express, 14*, 7821–7840.

Medeiros, F. A., Alencar, L. M., Zangwill, L. M., Bowd, C., Vizzeri, G., Sample, P. A., et al. (2009). Detection of progressive retinal nerve fiber layer loss in glaucoma using scanning laser polarimetry with variable corneal compensation. *Investigative Ophthalmology and Visual Science, 50*, 1675–1681.

Merino, D., Dainty, C., Bradu, A., & Podoleanu, A. G. (2006). Adaptive optics enhanced simultaneous *en-face* optical coherence tomography and scanning laser ophthalmoscopy. *Optics Express, 14*, 3345–3353.

Miller, D. T., Qu, J., Jonnal, R. S., & Thorn, K. (2003). Coherence gating and adaptive optics in the eye. In *Proceedings of SPIE Vol. 4956. Coherence domain optical methods and optical coherence tomography in biomedicine* (Vol. VII, pp. 65–72). Bellingham, WA: SPIE.

Miller, N. R., & George, T. W. (1978). Monochromatic (red-free) photography and ophthalmoscopy of the peripapillary retinal nerve fiber layer. *Investigative Ophthalmology and Visual Science, 17*, 1121–1124.

Monteiro, M. L. R., & Moura, F. C. (2008). Comparison of the GDx VCC scanning laser polarimeter and the stratus optical coherence tomography in the detection of band atrophy of the optic nerve. *Eye, 22*(5), 641–648.

Muramatsu, C., Hayashi, Y., Sawada, A., Hatanaka, Y., Hara, T., Yamamoto, T., et al. (2010). Detection of retinal nerve fiber layer defects on retinal fundus images for early diagnosis of glaucoma. *Journal of Biomedical Optics, 15*(1), 016021–016027.

Quigley, H. A., Reacher, M., Katz, J., Strahlman, E., Gilbert, D., & Scott, R. (1993). Quantitative grading of nerve fiber layer photographs. *Ophthalmology, 100*(12), 1800–1807.

Romero-Borja, F., Venkateswaran, K., Roorda, A., & Hebert, T. (2005). Optical slicing of human retinal tissue *in vivo* with the adaptive optics scanning laser ophthalmoscope. *Applied Optics, 44*, 4032–4040.

Roorda, A., Romero-Borja, F., Donnelly, W., III, Queener, H., Hebert, T., & Campbell, M. (2002). Adaptive optics scanning laser ophthalmoscopy. *Optics Express, 10*, 405–412.

Sakamoto, A., Hangai, M., Nukada, M., Nakanishi, H., Mori, S., Kotera, Y., et al. (2010). Three-dimensional imaging of macular retinal nerve fiber layer in glaucoma using spectral-domain optical coherence tomography. *Investigative Ophthalmology and Visual Science*. doi:10.1167/iovs.09-4954 (published ahead of print May 12).

Sehi, M., Ume, S., Greenfield, D. S., & Advanced Imaging in Glaucoma Study Group (2007). Scanning laser polarimetry with enhanced corneal compensation and optical coherence tomography in normal and glaucomatous eyes. *Investigative Ophthalmology and Visual Science, 48*, 2099–2104.

Seong, M., Sung, K. R., Choi, E. H., Kang, S. Y., Cho, J. W., Um, T. W., et al. (2010). Macular and peripapillary retinal nerve fiber layer measurements by spectral domain optical coherence tomography in normal-tension glaucoma. *Investigative Ophthalmology and Visual Science, 51*, 1446–1452.

Sommer, A., Katz, J., Quigley, H. A., Miller, N. R., Robin, A. L., Richter, R. C., et al. (1991). Clinically detectable nerve fiber atrophy precedes the onset of glaucomatous field loss. *Archives of Ophthalmology, 109*(1), 77–83.

Sommer, A., Miller, N. R., Pollack, I., Maumenee, A. E., & George, T. (1977). The nerve fiber layer in the diagnosis of glaucoma. *Archives of Ophthalmology, 95*(12), 2149–2156.

Torti, C., Považay, B., Hofer, B., Unterhuber, A., Carroll, J., Ahnelt, P. K., et al. (2009). Adaptive optics optical coherence tomography at 120,000 depth scans/s for non-invasive cellular phenotyping of the living human retina. *Optics Express, 17*, 19382–19400.

Varma, R., Skaf, M., & Barron, E. (1996). Retinal nerve fiber layer thickness in normal human eyes. *Ophthalmology, 103*, 2114–2119.

Wang, Y., Bower, B. A., Izatt, J. A., Tan, O., & Huang, D. (2007). *In vivo* total retinal blood flow measurement by Fourier domain Doppler optical coherence tomography. *Journal of Biomedial Optics, 12*, 041215.

Zawadzki, R. J., Cense, B., Zhang, Y., Choi, S. S., Miller, D. T., & Werner, J. S. (2008). Ultrahigh-resolution optical coherence tomography with monochromatic and chromatic aberration correction. *Optics Express, 16*, 8126–8143.

Zawadzki, R. J., Choi, S. S., Fuller, A. R., Evans, J. W., Hamann, B., & Werner, J. S. (2009). Cellular resolution volumetric *in vivo* retinal imaging with adaptive optics-optical coherence tomography. *Optics Express, 17*, 4084–4094.

Zawadzki, R. J., Choi, S. S., Jones, S. M., Oliver, S. S., & Werner, J. S. (2007). Adaptive optics-optical coherence tomography: Optimizing visualization of microscopic retinal structures in three dimensions. *Journal of the Optical Society of America A – Optics and Image Science, 24*, 1373–1383.

Zawadzki, R. J., Jones, S. M., Olivier, S. S., Zhao, M. T., Bower, B. A., Izatt, J. A., et al. (2005). Adaptive-optics optical coherence tomography for high-resolution and high-speed 3D retinal in vivo imaging. *Optics Express, 13*, 8532–8546.

Zhang, Y., Cense, B., Rha, J. T., Jonnal, R. S., Gao, W., Zawadzki, R. J., et al. (2006). High-speed volumetric imaging of cone photoreceptors with adaptive optics spectral-domain optical coherence tomography. *Optics Express, 14*, 4380–4394.

Zhang, Y., Rha, J. T., Jonnal, R. S., & Miller, D. T. (2005). Adaptive optics parallel spectral domain optical coherence tomography for imaging the living retina. *Optics Express, 13*, 4792–4811.